

Influence of Machine Integration on the Thermal Behavior of a PM Drive for Hybrid Electric Traction

Christian Paar, Annette Muetze, *Senior Member, IEEE*, and Hendrik Kolbe

Abstract—This paper describes a method for fast identification of the thermal behavior of vehicle integrated electric drives to propose a better understanding of electric machine design tailored to driving cycles. A simple, but satisfactorily accurate, calculation method for the estimation of machine losses, which is an input for the analytic thermal network, in the early design stage is introduced. The analytic models, which are verified using measurement data, are used for parameter and case studies for consideration of the thermal environment, with a focus on the gearbox. The first case study analyzes the influence of the gearbox on the thermal behavior of critical machine components. Aiming to use the gearbox lubricant for cooling the winding heads, an improvement of machine performance using an alternative cooling approach, which cools down the end windings, is shown in the second case study.

Index Terms—Gearbox, hybrid vehicle, oil cooling, permanent-magnet drive, thermal integration, thermal modeling.

I. INTRODUCTION

A. Motivation

A key design issue of electric drives for hybrid electric vehicles (HEVs) is the tradeoff between power density and performance. A special design challenge of drives for such applications is given by the driving profiles that can hardly be described by the definition of rated torque and speed, parameters with which electric machines have been specified for decades. The correlations between the electromagnetic design of electric machines and their cooling types have been investigated for a long time. Current approaches during the conceptual design and development phase typically meet the torque–speed requirements, which are defined by the application, e.g., by

oversizing the drive [1] (increased active length, reduced shear force density/torque density and current loading [2]) to exploit the thermal inertia for short-term overload operations and/or use costly high-temperature performance materials such as dysprosium [3]. Another approach to achieve packaging targets is the use of high-performance sheets (Fe–Co) to increase the possible air gap flux density [4], which also comes at the disadvantage of a higher price. Specific thermal optimization of the electric drive considering its thermal environment and operating profile allows a better meeting of customer requirements such as packaging, weight, performance, and costs. This thermal environment considers the mounting of the machine and thereby allows for exploitation of already existing thermal paths.

For HEV integrated electric drives, a definition of the electric drive's absolute maximum power may be derived using the hybridization factor [5], which differs depending on the HEV categories parallel, series, and parallel/series [6], i.e.,

$$HF = \frac{P_{EM}}{P_{EM} + P_{ICE}} \quad (1)$$

where P_{EM} and P_{ICE} are the maximum power of the electric machine and the internal combustion engine, respectively.

In addition to the drive train topology, another influencing factor that needs to be taken into account is the operating strategy of the vehicle [7]. All these factors influence the torque/speed load profile of the electric drive during vehicle operation. Integrating the drive into a hybrid electric drive train requires a holistic approach using real-world driving cycle thermal design.

The results we present aim to contribute to a better understanding of electric machine design tailored to the driving cycles and thermal environments as they occur with hybrid electric traction operation in the automotive field. The 50-kW peak electric drive discussed is designed for a plug-in HEV and allows for pure electric propulsion of the vehicle.

B. Approach

Such work requires the availability of a fast design process to enable a quick identification of thermal paths in the drive and at relevant mounting points. Different thermal models have been proposed for different applications. These include numerical and analytical lumped-parameter approaches [8]. As proposed in [9], numerical approaches such as computational

Manuscript received December 23, 2014; revised March 6, 2015; accepted April 20, 2015. Date of publication April 28, 2015; date of current version September 16, 2015. Paper 2014-IDC-1025.R1, presented at the 2014 IEEE Energy Conversion Congress and Exposition, Pittsburgh, PA, USA, September 20–24, and approved for publication in the IEEE TRANSACTIONS ON INDUSTRY APPLICATIONS by the Industrial Drives Committee of the IEEE Industry Applications Society. This work was supported in part by The Austrian Research Promotion Agency (FFG) and in part by the Styrian Business Promotion Agency (SFG).

C. Paar is with Project House EU, MAGNA Powertrain AG & Co KG, 8200 Albersdorf, Austria, and also with the Electric Drives and Machines Institute, Graz University of Technology, 8010 Graz, Austria (e-mail: christian.paar@magnapowertrain.com).

A. Muetze and H. Kolbe are with the Electric Drives and Machines Institute, Graz University of Technology, 8010 Graz, Austria (e-mail: muetze@tugraz.at; hendrik.kolbe@tugraz.at).

Color versions of one or more of the figures in this paper are available online at <http://ieeexplore.ieee.org>.

Digital Object Identifier 10.1109/TIA.2015.2427280

fluid dynamics (CFD) are suitable for detailed analysis of heat transmission such as the air gap or optimization of the air flow to improve the cooling [10] of the electric drive.

Lumped-parameter approaches are faster [11], but their challenge is the definition and computation of the parameters of the network [8].

Typically, the parameters are determined by dimensional information, using simulations or empirical correlations (e.g., [8] and [12]–[15]). Other studies that have been presented consider the thermal resistance of the air gap [16] or the winding [17]. The determination of the bearings thermal resistance is, for example, discussed in [15], [18], and [19]. Using these studies, as a starting point, we defined the thermal paths for our specific application regarding a hybrid electric drive.

Therefore, the chosen analytic modeling approach will be presented in Section II, and the model validation will be presented in Section III. Section IV discusses the gearbox integration, and Section V explores an alternative cooling approach using the gearbox lubricant.

The electric machine for the studies discussed is a 20-kW continuous-power interior-mounted permanent-magnet synchronous electric machine (IPM) with water jacket cooling. The IPM with a gearbox attached is mounted on the rear axle of a plug-in HEV. The IPM has a peak torque of 200 Nm during overload operation up to a shaft speed of 2380 r/min, the maximum speed is 12 000 r/min. The drive is disconnected at 15 000 r/min to allow for higher vehicle speeds (burst speed).

C. Integration Study Case 1: Gearbox

Aiming to study the thermal effects of drive integration in the vehicle environment, we investigate the influences of a gearbox mounted onto the drive end (DE), for different load scenarios.

Section IV discusses the influence of the gearbox on the end winding and magnet center temperatures, neglecting the thermal behavior of the gearbox itself.

D. Integration Study Case 2: Oil Spray Cooling

Section V considers the influence and capability of additional oil spray cooling of the end windings. Instead of cooling the stator back iron, as presented in [20], or the end windings by using an oil pump to generate automatic transmission fluid (ATF) spray [21], we added oil slingers for distributing a transmission fluid, which cools down the end windings. The oil slingers are mounted on the shaft near the winding heads.

II. MODELING APPROACH

A. Analytic Loss Model

To ensure fast parameter studies, an analytic approach is considered appropriate. The following loss sources are modeled as follows.

1) Winding Copper Losses (Joule Losses):

$$P_{cu} = m I_{ph}^2 R(\theta) k_s \quad (2)$$

where m is the number of phases, I_{ph} is the phase current, and $R(\theta)$ is the phase resistance, which depends on the temperature θ . Skin and proximity losses are considered by the correction factor k_s [22].

2) *Iron Losses*: For a fast computation of the iron losses in the different parts of the machine (core backs and teeth), the well-known Steinmetz equation [23] is used, i.e.,

$$P_{fe} = m p_{fe} \left(\frac{B}{B_{ref}} \right)^2 \left(\frac{f}{f_{ref}} \right)^{1.6} k_p \quad (3)$$

with flux density B , reference flux density B_{ref} , frequency f , reference frequency f_{ref} , and the factor k_p to take the degradation of the magnetic properties of the lamination material due to manufacturing into consideration. The modeling depth of the magnetic circuit for the calculation of the flux densities is determined by the geometric complexity of the flux paths. An appropriate calculation approach for the estimation of the machine losses is an equivalent circuit model similar to the one presented in [24], which describes the magnetic circuit by stator back iron, teeth, air gap, rotor yoke, and permanent-magnet equivalent reluctance.

3) *Magnets*: The eddy current losses in the magnets [24] are estimated according to [25]

$$P_{mag} = \frac{2bd}{\sigma\delta} |H|^2 \frac{b+a}{b} \quad (4)$$

where a , b , and d are the magnet dimensions, H is the magnetic field strength, δ is the skin depth, and σ is the electric conductivity. Finite element method (FEM) simulations of the realized machine showed that these losses are at approximately 1% of the total losses.

4) *Windage Losses*: The mechanical losses caused by air friction (windage losses) are modeled according to [2]

$$P_{m,air} = C_m v^2 d_R l_{fe} \quad (5)$$

where v is the surface speed, d_R is the rotor diameter, and l_{fe} is the stack length. The empirical value C_m is assumed at 8–10 for surface aeration and up to 15 for internal cooling [2].

5) *Electric Drive Mechanical Losses*: The losses that occur within the gearbox and those introduced into the system from additional loss sources (e.g., sealing rings) are taken from measurements. In particular, the sealing ring losses, windage losses, and bearing losses need special consideration as they occur on distributed locations within the drive and affect the loss distribution in the analytic model.

Therefore, we investigated these losses on a test bench with a dummy rotor (to avoid cogging torque). The measurements were carried out at different temperatures (from -25°C up to 120°C). The second step was the repetition of the test program with the seal rings removed. The third and last step was its repetition with the seal rings and the rotor removed. These measurements allow a separation of the gearbox, seal rings, windage, and bearing losses at the DE and the non-DE (NDE) (see Fig. 1).

The results (see Fig. 2) emphasize the significant influence of the temperature and the contribution of the sealing rings to the machine losses. For example, at -25°C and 48-km/h

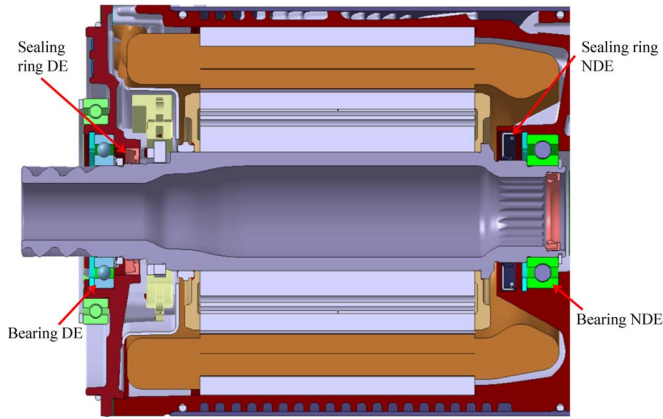


Fig. 1. Electric drive cross-section view, with location of bearings and sealing rings at NDE and DE.

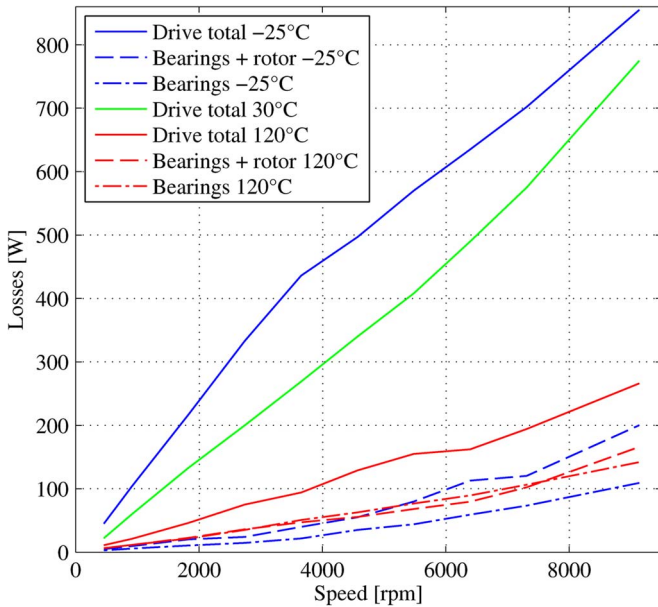


Fig. 2. Measured electric drive spin losses as a function of speed and temperature.

vehicle speed (4000 r/min), the sealing rings cause 91% of the mechanical losses. For higher temperatures, the sealing ring losses decrease, but the contribution of the bearing losses increases up to 53%.

6) *Gearbox Losses*: Traditionally, power losses in gearboxes are separated into no-load and load-dependent losses [26]. The load-dependent losses are caused by friction (teeth and bearings), and the no-load losses are mainly caused by oil splashing losses. For the integration study, the gearbox losses are measured for different temperatures (see Fig. 3).

These losses, which are implemented as lookup tables in the model, show nonlinear dependence on speed and temperature.

B. Thermal Model

The FEM and/or the CFD in combination with measurement data are used to determine selected heat transfer parameters

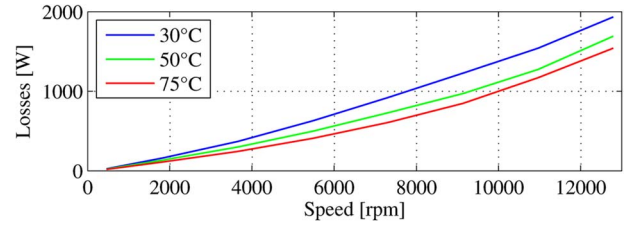


Fig. 3. Measured gearbox losses for different oil sump temperatures at zero torque.

(particularly if using a liquid- or air-cooled system) for the thermal model. As with the electromagnetic design, both analytic lumped circuit and numerical methods are available [8]. Both approaches require the definition of the thermal parameters, which is an involved task because of the complex materials and material combinations such as the laminated steel, impregnated wires, or wires with dual coating. Furthermore, not only thermal conduction occurs within the drive but also free and forced convections, as well as radiation. In addition, different types of cooling may be required to be investigated and compared.

Here, again, the approach of a lumped analytic model is taken, with certain parameters determined through numerical methods, measurements, and literature [12], [17], [27]. This allows determining the temperatures at selected points, such as the coolant temperature at the outer perimeter of the machine or the temperature in the center point of the magnets. The exact temperature distributions within certain parts of the machine, such as the magnets, cannot be computed with this approach, which is acceptable considering the focus of the presented work.

The lumped-parameter model developed for this study (see Fig. 4, baseline case) is designed to calculate the temperature at the following nodes: 0—node of average coolant temperature, 1—cooling jacket node, 2—point of average stator yoke temperature, 3—point of average teeth temperature, 4—boundary between stator teeth and air gap, 5—boundary between air gap and rotor surface, 6—virtual average rotor point, 7—virtual midpoint of bearing at NDE, 8—virtual midpoint of bearing at DE, 9—point of average winding temperature in stator slots, 10—point of average temperature of end winding (overhang) at NDE, 11—point of average temperature of end winding at DE, 12—point of average shaft surface temperature, 13—virtual point within frame between equivalent axial and radial sections at NDE, 14—virtual point within frame between equivalent axial and radial sections at DE, 15—virtual point in air volume in end-winding region at NDE, 16—virtual point in air volume in end-winding region at DE, 17—virtual point of average side surface temperature of rotor at NDE, 18—virtual point of average side surface temperature of rotor at DE, 19—virtual point of average surface temperature of end winding at NDE, 20—virtual point of average surface temperature of end winding at DE.

The following thermal capacitances are modeled: C_1 —frame (and mounted parts), C_2 —stator yoke, C_3 —stator teeth, C_6 —rotor, C_7/C_8 —bearings, C_9 —slots, C_{10} —end winding at NDE, C_{11} —end winding at DE, C_{12} —shaft, C_{15} inner air at NDE, C_{16} —inner air at DE.

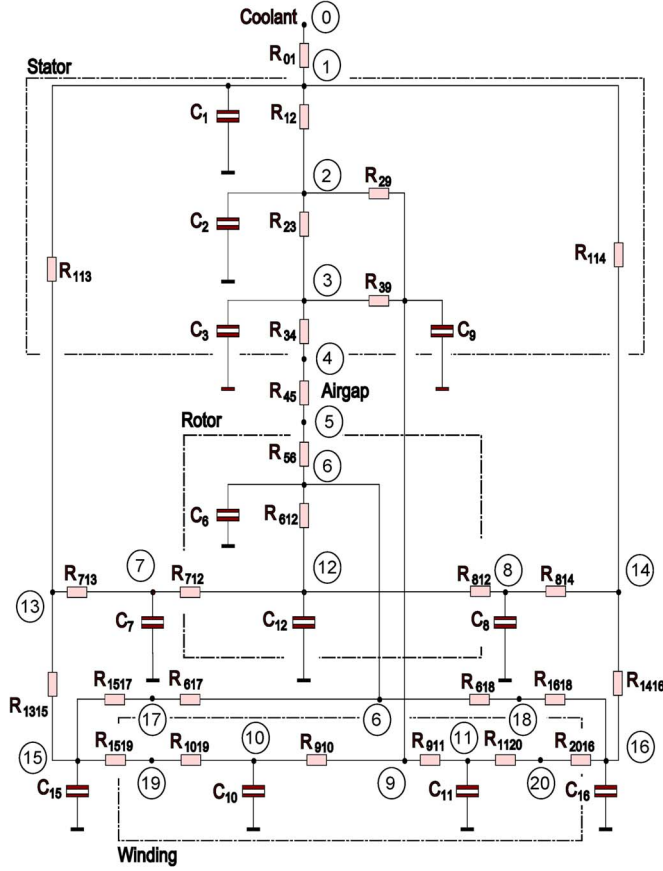


Fig. 4. Thermal lumped-parameter model.

This lumped-parameter model may be mathematically summarized as [28], [29]

$$\underline{C} \frac{d\vec{\theta}(t)}{dt} = \vec{P} - \underline{G}\vec{\theta}(t) \quad (6)$$

with the vector of loss injections \vec{P} , the conductivity matrix \underline{G} , the temperature vector

$$\vec{\theta}(t) = \begin{pmatrix} \theta_1(t) \\ \theta_2(t) \\ \theta_3(t) \\ \vdots \\ \theta_i(t) \end{pmatrix} \quad (7)$$

and the diagonal matrix \underline{C} which defines the capacitance for each node, as indicated in Fig. 4. The model is solved in MATLAB/Simulink.

The thermal conductivities in matrix \underline{G} are series and parallel resistances of equivalent thermal resistances defined by contact resistance, convection, and radiation. The contact and/or the convection conductance is defined as

$$G = hA \quad (8)$$

with surface area A and the effective contact or convection heat transfer coefficient h . This thermal lumped-parameter model assumes that the heat transfers in the radial and axial directions can be treated independently from each other [12]. As

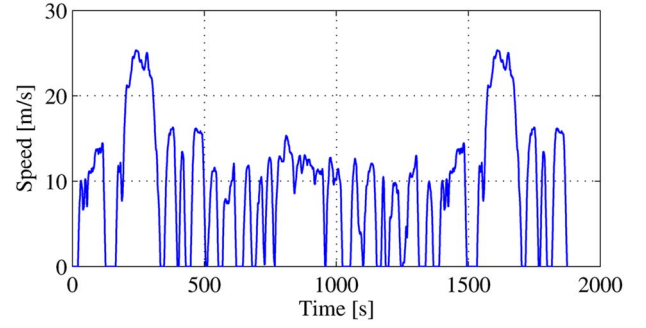


Fig. 5. FTP-75 speed profile.

a direct consequence, different heat flow paths, for instance, heat flow in axial and radial directions, can be treated as problems related to 1-D heat transfer. Of critical importance is the correct connection of the different paths, i.e., the thermal resistances, thermal capacitances, and power injections of the corresponding elements in the lumped-parameter model.

C. Vehicle Model and Driving Cycles

Relevant driving cycles for governmental emission homologation of vehicles are the New European Driving Cycle (NEDC) for the European Union (EU) and the Federal Test Procedure (FTP-75) for the U.S. The fuel and emission regulations depend on national legislations [30], [31]. Furthermore, in the future (as proposed by the EU parliament), the Worldwide Harmonized Light Vehicles Test Procedure may be relevant [30].

In this paper, FTP-75 (see Fig. 5) was considered, because it requires higher torque dynamics to fulfill the speed target over time, when compared with NEDC.

For the calculation of the electric drive torque profile, a simple longitudinal vehicle model using a quasi-static approach was used [32]. The quasi-static vehicle model calculates the torque profile for the electric drive from a given speed profile without considering dynamic effects in the vehicle drive train. Focusing on the electric drive, hybrid vehicle control strategies were not considered. The midsize car simulated has a curb weight of $m_c = 2058$ kg. A load (driver) weight of $m_l = 75$ kg was assumed for the simulations to calculate the total driving force

$$F_v = m_v g \mu_r + \frac{A_v v_v^2 \rho c_w}{2} + (m_c f_{\text{rot}} + m_l) \dot{v}_v \quad (9)$$

with vehicle speed v_v , air density ρ , total vehicle weight $m_v = m_c + m_l$, and force of gravity $g = 9.81$ m/s². The rolling friction constant, which depends on the road surface to wheel contact, was assumed with $\mu_r = 0.008$. The vehicle cross-sectional area is $A_v = 2.28$ m², with a drag coefficient of $c_w = 0.29$. The factor f_{rot} is a simplification to consider the rotational masses (inertia) of the drive train as a percentage share of the curb weight and was estimated with 5% of the curb weight ($f_{\text{rot}} = 1.05$). The total driving force is used to calculate the required shaft torque of the electric drive via the tire radius. The front/rear torque distribution of the vehicle is defined with 40% : 60% in the simulations.

TABLE I
COMPARISON OF TOTAL LOSSES: DATA OBTAINED FROM FEM,
LOSS MODEL, AND MEASUREMENT RESULTS

	FEM	Meas.	Model	Difference Model & Meas.
250 rpm 200 Nm	5741 W	5933 W	5706 W	-3.83 %
2000 rpm 200 Nm	6245 W	6327 W	6073 W	-4.00 %
4000 rpm 60 Nm	1130 W	1138 W	1167 W	-2.55 %
7000 rpm 20 Nm	917 W	918 W	906 W	-1.27 %
11000 rpm 20 Nm	2107 W	2073 W	1916 W	-8.20 %

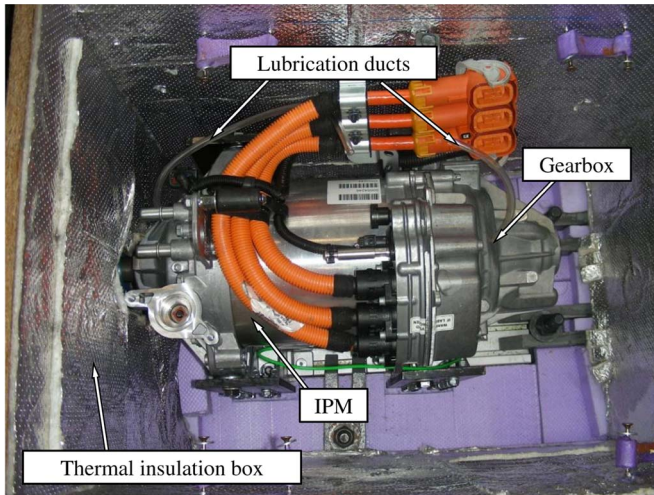


Fig. 6. Test rig with thermal insulation box and lubrication tubes.

III. MODEL VALIDATION

A. Validation of the Loss Model

For the validation of the loss model, measurements are used to verify the overall model accuracy. Table I shows the results for selected operating points. They illustrate the overall model accuracy in a wide torque and speed range. The proposed analytic approach shows a sufficient agreement with measured data and FEM model results. The differences are caused by the proposed analytic calculation approach of the core losses (see Section II-A). Note also that the difference between the measurement results and the FEM simulation results is smaller.

To ensure accurate computation of the temperatures at the different points considered in the model, the loss distribution in the electric drive must be also considered. The mechanical losses were determined using the test rig (see Fig. 6).

The relative distribution of the iron losses within the machine is not discussed in detail at this point, because their accurate consideration is also reflected by the computed temperatures. The experimental validation of the temperature model is discussed in the following section.

B. Validation of the Temperature Model

Table II compares the measured data and the analytic simulation results for four different operating points (steady state).

TABLE II
MEASURED AND COMPUTED TEMPERATURES
AT DIFFERENT OPERATING POINTS

	1000 rpm, 90 Nm		2150 rpm, 90 Nm	
	Meas.	Model	Meas.	Model
Winding, slot	118.0 °C	116.4 °C	123.5 °C	116.1 °C
Winding, NDE	113.9 °C	126.0 °C	117.6 °C	124.8 °C
Winding, DE	126.6 °C	126.1 °C	132.5 °C	124.7 °C
Coolant outlet	69.7 °C	70.1 °C	70.5 °C	70.2 °C
Rotor	71.4 °C	97.4 °C	77.9 °C	95.5 °C
	6000 rpm, 32 Nm		12000 rpm, 17 Nm	
	Meas.	Model	Meas.	Model
Winding, slot	88.6 °C	81.4 °C	111.6 °C	99.6 °C
Winding, NDE	85.5 °C	82.4 °C	103.7 °C	99.9 °C
Winding, DE	89.3 °C	82.6 °C	112.4 °C	100.5 °C
Coolant outlet	67.0 °C	66.6 °C	69.6 °C	69.1 °C
Rotor	74.8 °C	82.6 °C	88.4 °C	105.5 °C

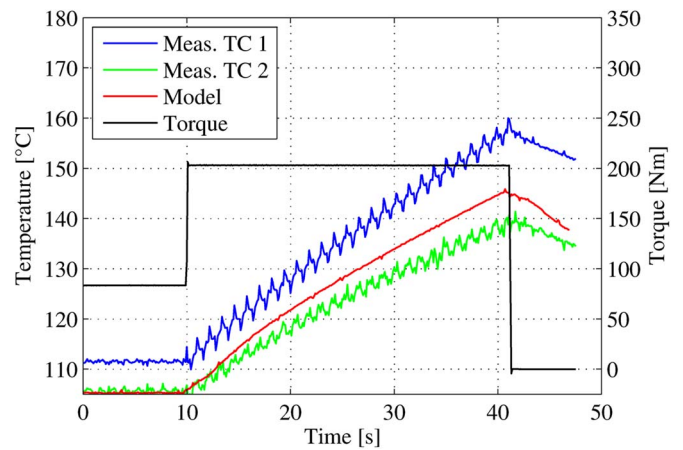


Fig. 7. Winding in slot temperature: thermal transient 30-s peak torque step response at 250 r/min.

Relevant points are the DE and NDE end winding, the winding temperature in the slots, and the rotor (respectively, magnet) temperature. Note that these results already indicate the important role of the end windings both at the NDE and at the DE of the machine; these are the machine hot spots.

The modeled rotor temperature is higher than the measured one (see Table II): As the bearings are lubricated by the attached gearbox through special oil ducts, the test rig was set up to ensure a defined lubrication of the bearings with 39-ml/min lube supply for each bearing using lubrication tubes (see Fig. 6). The temperature of the oil sump was measured. From the change of temperature of oil flowing out of the bearings, a negative heat flow was determined (see nodes 7 and 8 in Fig. 4). However, this defined lubrication flow does not correspond to the lubrication situation with the gearbox attached; therefore, this difference between measured and modeled rotor temperatures is considered acceptable.

Figs. 7 and 8 show the behavior under dynamic operating conditions, to represent the transient validation. The electric drive was warmed up at 90 Nm and 1000 r/min until the end-winding temperatures had reached a steady-state temperature of 120 °C. Then, a 200 Nm peak torque step at 250 r/min (see Fig. 7) and 2380 r/min (see Fig. 8) was applied for 30 s.

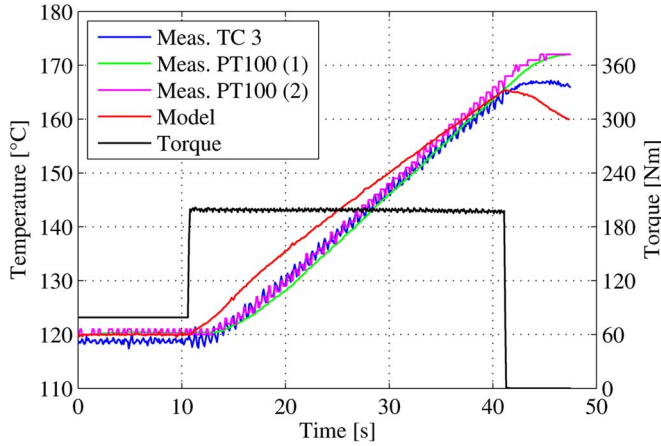


Fig. 8. Winding head DE side: thermal transient 30-s peak torque step response at 2380 r/min.

Fig. 7 compares the temperature computed for the winding in the slots with those two measured by thermocouples (TCs). The difference is considered acceptable because of the different measurement locations within the slots: The lumped-parameter model only represents a mean temperature for the slot winding temperature.

Fig. 8 compares the temperature computed for the winding head at the DE with those measured with a TC and two PT100 at different locations within the winding head. Both step responses indicate sufficient accuracy of the modeled thermal time constants and thermal capacitances.

IV. INTEGRATION STUDY CASE 1: GEARBOX

A. Simulation Approach

In this case study, we consider the gearbox losses and their influence on the electric drive's thermal behavior. The thermal behavior of the gearbox is not part of the thermal model presented in Fig. 4. The gearbox losses are injected into the model at corresponding frame and shaft nodes.

Since the gearbox is thermally connected both to the shaft and the housing, the loss distribution within the gearbox is required. The loss generation and distribution within the gearbox is affected by a variety of parameters such as the local speed dependent oil flow distribution [33], [34], the thermal characteristics of the contact zone (teeth) and related contact-generated heat [35], and the surface roughness of the gearbox housing. These parameters are part of the lubrication and gearbox development process and were not explicitly determined for the scope of this work, but are estimated based on the temperature distribution within gearboxes, as discussed in [33]–[36]. We assume a fixed distribution, where 40% of the losses flow into the shaft, and 60% flow into the frame.

B. Scenario I: Boost Cycle

Based on the gearbox measurements (see Section II-A), we discuss an exemplary driving scenario: starting from a no-load operating point at 2380 r/min and a gearbox temperature of

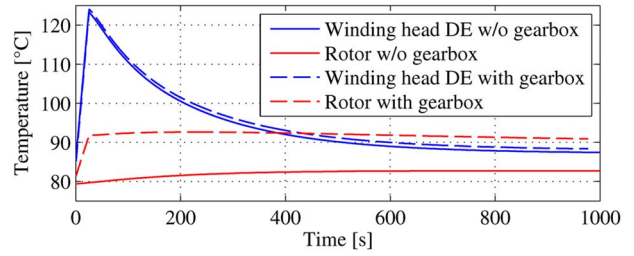


Fig. 9. Comparison: influence of gearbox losses for end-winding and magnet temperatures for a 25-s boost cycle.

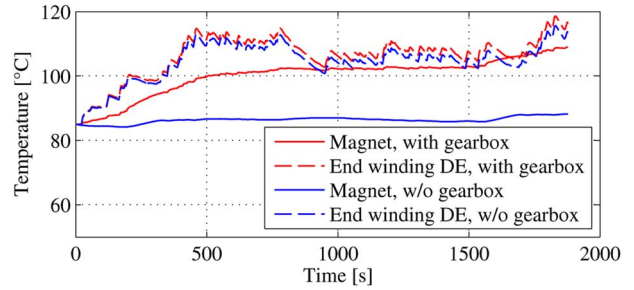


Fig. 10. Comparison: magnet and end-winding temperatures at DE with and without consideration of gearbox.

60 °C, a boost cycle with 200 Nm is applied for 25 s. Then, the gearbox contributes additional 3400-W losses, which are 60% of the total machine losses (including bearing and ventilation) in this operating point. For the calculation of the steady-state operating point, the spin losses of the gearbox were considered. During the boost cycle, the additional load-dependent losses were also taken into account. The computed end-winding and magnet temperatures are shown in Fig. 9.

Under these conditions, the average end-winding temperature of both sides reaches a maximum of 124 °C (NDE–DE difference: 1 K) after 25 s. This is only 0.7 K higher than the mean winding temperature without consideration of the gearbox (baseline). Thus, for this specific drive, the additional heat introduced by the gear box losses does not affect the end-winding temperature significantly.

The situation is, however, very different for the magnets. The additional heat flow from the rotor due to the gear box increases the temperature of the magnets by 12 K (see Fig. 9). This may, in turn, severely impede the performance of the motor, as the magnets may provide less magnetic flux, and more phase current might be required for the desired torque to be produced, increasing the losses and thus the heat development further.

C. Scenario II: FTP-75

To evaluate gearbox influence on the rotor temperature during a driving cycle, the specified setup was simulated with and without the gearbox using the vehicle model introduced in Section II-C.

Fig. 10 indicates the significant influence the gearbox losses may have on the magnet temperature. The magnet temperature after the cycle is 21 K higher if gearbox losses are considered. However, the temperature remains below the critical limits.

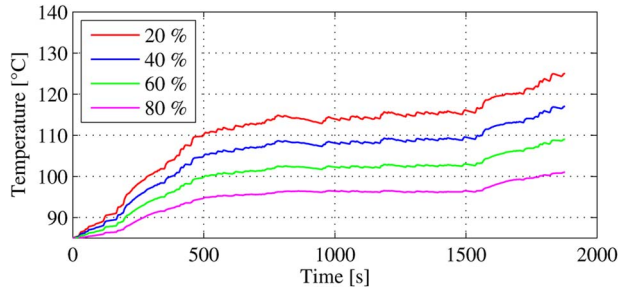


Fig. 11. Magnet temperature for different loss distributions within the gearbox (ratio frame to shaft).

D. Scenario III: Variation of Gearbox Heat Flow

As indicated earlier (see Section IV-A), the distribution of the gearbox losses between the frame and the shaft of the machine may only be known with a certain degree of accuracy and serves as an additional parameter to consider during the design process of an integrated drive, to reduce possible thermal stress on the magnets. (Note that, since the winding-head temperature is only slightly affected by the attached gearbox, this temperature is not analyzed further here.)

The analysis of the magnet temperatures for different frame-to-shaft heat distribution factors is shown in Fig. 11. The design of the gearbox may significantly influence the rotor temperature. The design of the distribution of the gearbox losses between the machine frame and the shaft may provide an additional degree of freedom during the development of integrated drives, allowing for reduction of the thermal stress on the magnets.

V. INTEGRATION STUDY CASE 2: OIL SPRAY COOLING

A. Evaluation of Potential

The influence of oil-cooled end windings (splash-oil cooling) was studied. The heat transfer coefficients were taken from the literature [21]. The heat transfer coefficient between the oil (ATF) and the end winding is a nonlinear function of the temperature [21]. For the range of temperatures occurring within this study, it varies between 100 W/m²K at 40 °C and 200 W/m²K at 80 °C, up to 300 W/m²K at 100 °C oil temperature.

As in the previous case, a 25-s torque step, starting from the nominal operating point at steady state, is applied.

For example, an oil spray temperature (ATF as cooling fluid) of 80 °C decreases the maximum temperature of the end winding by 19 K, from 165 °C down to 146 °C, whereas that of the winding in the slots decreases only by 6 K, from 147 °C down to 138 °C.

Fig. 12 shows the difference between the baseline case (no gearbox, no oil-spray cooling on end winding) and the effect of oil-spray cooling for different ATF temperatures.

The increasing heat transfer coefficient with increasing cooling fluid temperatures may suggest that the largest effect would be obtained at high oil temperatures. However, high cooling fluid temperatures heat up the system. Therefore, the largest cooling effort can be obtained for a fluid temperature of 80 °C.

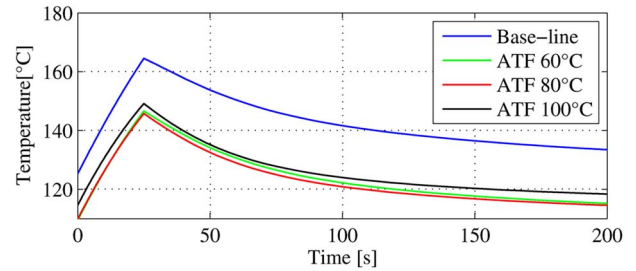


Fig. 12. Simulated: comparison of end-winding temperatures during boost cycle.

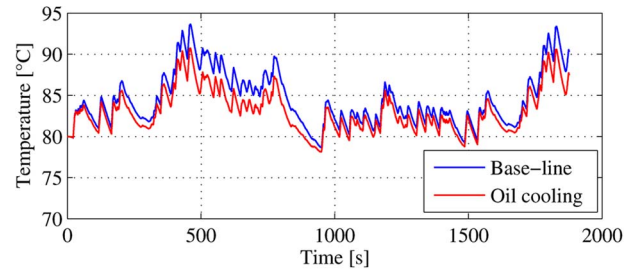


Fig. 13. Simulated: comparison of end-winding DE temperature with and without oil cooling.

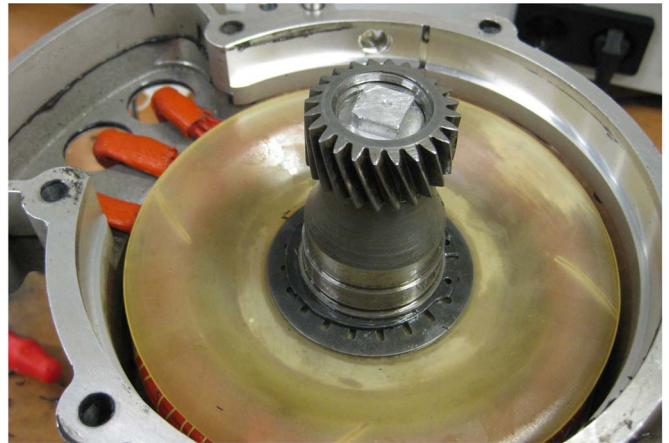


Fig. 14. Splash-oil-cooled IPM.

This temperature is the best compromise between fluid temperature and heat transfer coefficient.

To conclude this study, the drive performance with ATF cooling at 80 °C was simulated for the FTP-75 driving cycle (see Fig. 13), the improvement was emphasized. The end winding at the drive side has a 3 K lower temperature; the rotor temperature is only 0.3 K lower and therefore not affected by the oil cooling.

B. Proof of Concept

To prove the identified cooling potential, a prototype drive with a special oil distribution plate (oil slinger, see Fig. 14) was developed. This oil slinger plunges in an oil sump with special cooling fluid (with lubrication properties) to generate oil spray caused by the rotation of the oil slinger.

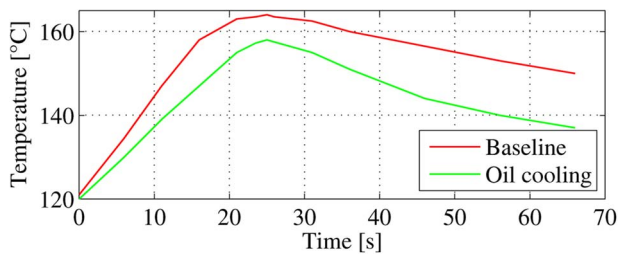


Fig. 15. Measured: comparison of baseline IPM and oil-cooled prototype at 180 Nm, 200-r/min torque step.

Fig. 15 shows the measurement results of this improved cooling effort at an operation speed of 200 r/min and a 20-s 180 Nm torque step. The oil fog caused by the oil slinger cools down the end winding by 6 K. The oil sump temperature at the test rig was 105 °C. This adaption increases the possible boost time of the IPM, as the winding heads are the hot spot of the machine. If we compare the measurement results with the theoretically identified cooling potential, the realized improvement is slightly lower than expected. This is attributed to the additional splashing losses caused by the oil slingers.

These additional (measured) speed-dependent losses caused by the movement of the fluid are in the range of 250 W at 3000 r/min and 750 W at 6000 r/min without oil (air friction). With oil, the spin losses are in the range of 500 W at 2000 r/min to 1870 W at 6000 r/min. Within this speed range, the losses increase linearly with speed.

VI. CONCLUSION

Aiming to study the thermal effects of drive integration in a vehicle environment, the possible influences of a gearbox and oil-spray cooling on the thermal behavior of an IPM machine for electric traction applications are computed. To this aim, a fast analytic approach has been developed that draws from a model that had been validated experimentally. The vehicle model follows a quasi-static approach to speed up the simulation and allow for future parameter studies. The studies illustrate the role that drive integration may play in thermal studies of electric drives, notably the consideration of additional heat sinks/sources exterior to the main machine. The temperature of the magnets was 21 K higher with the gearbox attached. Direct end-winding cooling allowed for a temperature reduction of 6 K.

REFERENCES

- [1] C. M. Liao, C. L. Chen, and T. Katcher, "Thermal analysis for design of high performance motors," in *Proc. 6th ITherm*, 1998, pp. 424–433.
- [2] J. Willberger, "AC motor design and evaluation for automotive traction applications," Ph.D. dissertation, Graz Univ. Technol., Graz, Austria, Dec. 2011.
- [3] K. Bennion, Electric motor thermal management. May 2013. [Online]. Available: http://energy.gov/sites/prod/files/2014/03/f13/ape030_bennion_2013_o.pdf
- [4] I. Adcock, "Winning the power struggle," in *Proc. Autom. Design, Pan-Eur. Mag. SAE Int.*, Apr. 2012, pp. 12–15. [Online]. Available: www.sae.org/magazines/pdf/AUTODES0412.pdf
- [5] S. Lukic and A. Emadi, "Effects of drivetrain hybridization on fuel economy and dynamic performance of parallel hybrid electric vehicles," *IEEE Trans. Veh. Technol.*, vol. 53, no. 2, pp. 385–389, Mar. 2004.
- [6] S. Lukic, J. Cao, R. Bansal, F. Rodriguez, and A. Emadi, "Energy storage systems for automotive applications," *IEEE Trans. Ind. Electron.*, vol. 55, no. 6, pp. 2258–2267, Jun. 2008.
- [7] S. Wirasingha and A. Emadi, "Classification and review of control strategies for plug-in hybrid electric vehicles," *IEEE Trans. Veh. Technol.*, vol. 60, no. 1, pp. 111–122, Jan. 2011.
- [8] A. Boglietti *et al.*, "Evolution and modern approaches for thermal analysis of electrical machines," *IEEE Trans. Ind. Electron.*, vol. 56, no. 3, pp. 871–882, Mar. 2009.
- [9] C. Jungreuthmayer *et al.*, "A detailed heat and fluid flow analysis of an internal permanent magnet synchronous machine by means of computational fluid dynamics," *IEEE Trans. Ind. Electron.*, vol. 59, no. 12, pp. 4568–4578, Dec. 2012.
- [10] J. Dong, Y. Huang, L. Jin, H. Lin, and H. Yang, "Thermal optimization of a high-speed permanent magnet motor," *IEEE Trans. Magn.*, vol. 50, no. 2, pp. 749–752, Feb. 2014.
- [11] N. Bracikowski, M. Hecquet, P. Brochet, and S. V. Shirinskii, "Multiphysics modeling of a permanent magnet synchronous machine by using lumped models," *IEEE Trans. Ind. Electron.*, vol. 59, no. 6, pp. 2426–2437, Jun. 2012.
- [12] P. H. Mellor, D. Roberts, and D. R. Turner, "Lumped parameter thermal model for electrical machines of TEFC design," *Proc. Inst. Elect. Eng.*, vol. 138, no. 5, pp. 205–218, Sep. 1991.
- [13] A. Boglietti, A. Cavagnino, and D. Staton, "Determination of critical parameters in electrical machine thermal models," in *Conf. Rec. IEEE IAS Annu. Meeting*, Sep. 2007, pp. 73–80.
- [14] A. Boglietti, A. Cavagnino, M. Lazzari, and M. Pastorelli, "A simplified thermal model for variable-speed self-cooled industrial induction motor," *IEEE Trans. Ind. Appl.*, vol. 39, no. 4, pp. 945–952, Jul./Aug. 2003.
- [15] D. Staton, A. Boglietti, and A. Cavagnino, "Solving the more difficult aspects of electric motor thermal analysis in small and medium size industrial induction motors," *IEEE Trans. Energy Convers.*, vol. 20, no. 3, pp. 620–628, Sep. 2005.
- [16] D. Howey, P. Childs, and A. Holmes, "Air-gap convection in rotating electrical machines," *IEEE Trans. Ind. Electron.*, vol. 59, no. 3, pp. 1367–1375, Mar. 2012.
- [17] N. Simpson, R. Wrobel, and P. Mellor, "Estimation of equivalent thermal parameters of impregnated electrical windings," *IEEE Trans. Ind. Appl.*, vol. 49, no. 6, pp. 2505–2515, Nov./Dec. 2013.
- [18] S. Isert, "Heat transfer through a rotating ball bearing," M.S. thesis, Utah State Univ., Logan, UT, USA, 2011.
- [19] Y. R. Takeuchi, M. A. Eb, B. A. Blake, S. M. Demsk, and J. T. Dickef, "Influence of oil lubrication on spacecraft bearing thermal conductance," in *Proc. 38th Aerosp. Mechanisms Symp.*, 2006, pp. 291–302. [Online]. Available: <http://www.esmats.eu/amspapers/completelist.php?whichYear=2006>
- [20] Z. Huang, S. Nategh, M. Alakula, V. Lassila, and J. Yuan, "Direct oil cooling of traction motors in hybrid drives," in *Proc. IEEE IEVC*, 2012, pp. 1–8.
- [21] M. Kamiya, Y. Kawase, T. Kosaka, and N. Matsui, "Temperature distribution analysis of permanent magnet in interior permanent magnet synchronous motor considering PWM carrier harmonics," in *Proc. ICEMS*, 2007, pp. 2023–2027.
- [22] G. Mueller, K. Vogt, and B. Ponick, *Berechnung Elektrischer Maschinen*, 6th ed. Weinheim, Germany: Wiley-VCH Verlag, 2008.
- [23] C. P. Steinmetz, "On the law of hysteresis," *AIEE Trans.*, vol. IX, no. 1, pp. 619–758, Jan. 1892.
- [24] T. J. E. Miller, *Speed's Electric Motors: An Outline of Some of the Theory in the Speed Software for Electric Machine Design With Problems and Solutions*. Hillsboro, OH, USA: Magna Physics, 2004.
- [25] K. Yamazaki and A. Abe, "Loss investigation of interior permanent-magnet motors considering carrier harmonics and magnet eddy currents," *IEEE Trans. Ind. Appl.*, vol. 45, no. 2, pp. 659–665, Mar./Apr. 2009.
- [26] J. Wang, X. Wang, Y. Ma, N. Liu, and Z. Yang, "Analysis of heat transfer in power split device for hybrid electric vehicle using thermal network method," *Adv. Mech. Eng.*, vol. 2014, pp. 1–9, 2014.
- [27] J. Guosheng, D. Liyong, and K. Ken, *Advanced Thermal Management Materials*. New York, NY, USA: Springer-Verlag, 2013, vol. VIII.
- [28] B.-H. Lee, K.-S. Kim, J.-W. Jung, J.-P. Hong, and Y.-K. Kim, "Temperature estimation of IPMSM using thermal equivalent circuit," *IEEE Trans. Magn.*, vol. 48, no. 11, pp. 2949–2952, Nov. 2012.
- [29] Y. Bertin, E. Videcoq, S. Thieblin, and D. Petit, "Thermal behavior of an electrical motor through a reduced model," *IEEE Trans. Energy Convers.*, vol. 15, no. 2, pp. 129–134, Jun. 2000.

- [30] UNECE, Working Party on Pollution and Energy (GRPE), Accessed on Jun. 7, 2014. [Online]. Available: http://www.unece.org/trans/main/wp29/wp29wgs/wp29grpe/wltp_dhc11.html
- [31] EPA, Federal Test Procedure Revisions, Accessed on Jun. 7, 2014. [Online]. Available: <http://www.epa.gov/otaq/sftp.htm#cycles>
- [32] L. Guzzella and A. Amstutz, The QSS Toolbox Manual, 2005, Accessed on Jun. 7, 2014. [Online]. Available: http://www.idsc.ethz.ch/content/dam/ethz/special-interest/mavt/dynamic-systems-n-control/idsc-dam/Research_Onder/Downloads/qss.zip
- [33] F. V. G. Leprince, C. Changenet and P. Velex, "Investigations on oil flow rates projected on the casing walls by splashed lubricated gears," *Adv. Tribology*, vol. 2012, 2012, Art. ID 365414.
- [34] L. Manin and D. Play, "Thermal behavior of power gearing transmission, numerical prediction, and influence of design parameters," *J. Tribology*, vol. 121, no. 4, pp. 693–702, Oct. 1999.
- [35] M. Yazdani and M. C. Soteriou, "A novel approach for modeling the multiscale thermo-fluids of geared systems," *Int. J. Heat Mass Transfer*, vol. 72, pp. 517–530, May 2014. [Online]. Available: <http://www.sciencedirect.com/science/article/pii/S0017931014000635>
- [36] M. Yazdani, M. C. Soteriou, F. Sun, and Z. Chaudhry, "Prediction of the thermo-fluids of gearbox systems," *Int. J. Heat Mass Transfer*, vol. 81, pp. 337–346, Feb. 2015. [Online]. Available: <http://www.sciencedirect.com/science/article/pii/S0017931014009235>



Christian Paar received the B.Sc. degree in mechatronics and microsystems engineering and the M.Sc. degree in mechatronics from the University of Applied Sciences, Wiener Neustadt, Austria, in 2009 and 2011, respectively. He is currently working toward the Ph.D. degree at Graz University of Technology, Graz, Austria.

He is also currently a mechatronic engineer with MAGNA Powertrain AG & Co KG, Albersdorf, Austria. His research focuses on the improvement of the thermal behavior of electric traction drives for

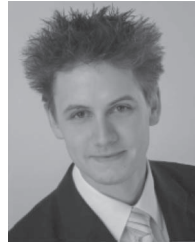
hybrid electric and electric vehicles.



Annette Muetze (S'03–M'04–SM'09) received the Dipl.-Ing. degree in electrical engineering from Darmstadt University of Technology, Darmstadt, Germany, in 1999, the Diploma degree in general engineering from the Ecole Centrale de Lyon, Ecully, France, in 1999, and the Dr.-Ing. degree in electrical engineering from Darmstadt University of Technology in 2004.

She is currently a Full Professor with Graz University of Technology, Graz, Austria, where she heads the Electric Drives and Machines Institute.

Prior to joining Graz University of Technology, she was an Assistant Professor with the Department of Electrical and Computer Engineering, University of Wisconsin–Madison, Madison, WI, USA, and an Associate Professor with the School of Engineering, University of Warwick, Coventry, U.K.



Hendrik Kolbe received the Dipl.-Ing. degree in electrical engineering and information technology from RWTH Aachen University, Aachen, Germany, in 2010.

Until 2014, he was a Research Assistant with Graz University of Technology, Graz, Austria, where he focused on the thermal modeling of electric machines. He is currently working on electric power-assisted steering systems in industry.